

## Article

# Reaction Characteristics of Two Types of Shale with Supercritical CO<sub>2</sub> and Its Potential Impact on Flow-Back Strategies

Wei Yan <sup>1,\*</sup>, Guangyao Leng <sup>1</sup>, Wenbo Li <sup>2</sup>, Tao Wu <sup>3</sup>, Mustajab Safarov <sup>1</sup>, Jean P. E. Amboulou Ndessabeka <sup>1</sup> and Keyu Meng <sup>4</sup>

<sup>1</sup> State Key Laboratory of Petroleum Resource and Prospecting, China University of Petroleum, Beijing 102249, China

<sup>2</sup> Tianjin Branch, CNOOC Co., LTD., Tianjin 300452, China

<sup>3</sup> Chuanqing Drilling Engineering Co., LTD., CNPC, Xi'an 710018, China

<sup>4</sup> Petroleum Engineering School, Southwest Petroleum University, Chengdu 610500, China

\* Correspondence: yanwei@cup.edu.cn



**Citation:** Yan, W.; Leng, G.; Li, W.; Wu, T.; Safarov, M.; Ndessabeka, J.P.E.A.; Meng, K. Reaction Characteristics of Two Types of Shale with Supercritical CO<sub>2</sub> and Its Potential Impact on Flow-Back Strategies. *Minerals* **2022**, *12*, 1459. <https://doi.org/10.3390/min12111459>

Academic Editors: Barbara Cantucci and Giordano Montegrossi

Received: 19 September 2022

Accepted: 15 November 2022

Published: 18 November 2022

**Publisher's Note:** MDPI stays neutral with regard to jurisdictional claims in published maps and institutional affiliations.



**Copyright:** © 2022 by the authors. Licensee MDPI, Basel, Switzerland. This article is an open access article distributed under the terms and conditions of the Creative Commons Attribution (CC BY) license (<https://creativecommons.org/licenses/by/4.0/>).

**Abstract:** Supercritical carbon dioxide (SC-CO<sub>2</sub>) fracturing has been used in developing low permeability and water-sensitive reservoirs in recent years, which is expected to become a new generation of unconventional reservoir fracturing fluid. However, the water-rock interaction characteristics of various lithology shales under SC-CO<sub>2</sub> circumstance and its influence on fracturing effect still need to be investigated. Two kinds of shale samples from C7 and S1 formations of the Ordos Basin were treated by SC-CO<sub>2</sub> with formation water. The aims of the research are to determine the processes taking place in shale reservoir when considering minerals components transformation, porosity/permeability variation, and micro pore-structure change during the SC-CO<sub>2</sub> fracturing. Static and dynamic SC-CO<sub>2</sub> immersed experiments were conducted and the scanning of electron microscopy (SEM) and X-ray diffraction (XRD) was employed to analyze the surface morphology and newly formed minerals. Helium porosimeter, the ultralow permeability meter, and the CT scanner are employed to record the alternation of physical parameters during SC-CO<sub>2</sub> dynamic injection. The experimental results show that the C7 samples are rich of chlorite and easily reacting with SC-CO<sub>2</sub> saturated formation water to form new minerals, but the S1 samples are insensitive to aqueous SC-CO<sub>2</sub>. The minimum value of permeability and porosity of the C7 cores appear at 24h in the long-interval experiment, but in the short-interval dynamic experiment, the minimum values move ahead to 12h. The optimal flowback time for the C7 reservoir is before 12 h or after 24 h. The high-pressure SC-CO<sub>2</sub> flooding pushes the new forming minerals particles to migrate to the outlet side and block the pore throat. For the S1 core results, the porosity and permeability change little in both short and long interval experiments. There is no strict flow-back time requirement for S1 reservoir during SC-CO<sub>2</sub> fracturing. This study is significance for the efficient application of SC-CO<sub>2</sub> in the exploitation of shale oil reservoirs.

**Keywords:** shale oil; SC-CO<sub>2</sub> fracturing; CO<sub>2</sub>-water-rock interaction; micro-pore structure; flow-back time

## 1. Introduction

As conventional resources tend to fall into depletion, a large amount of attention has been paid to unconventional resources. Currently, large-scale hydraulic fracturing is considered the most common method of developing unconventional oil and gas fields [1–3]. However, it will have a series of consequences when a large amount of water-based fracturing fluid is used in the oil and gas development process. For example, it will cause a shortage of water resources, notably in areas where there are droughts and water shortages, and it will cause swelling of clay minerals and cause formation damage for the formation with high clay mineral content. Furthermore, hydraulic fracturing will also lead to

groundwater pollution [4–6]. To eliminate above mentioned problems, supercritical carbon dioxide (SC-CO<sub>2</sub>) has been proposed as an anhydrous fracturing fluid in the development of unconventional oil and gas fields, because it can solve problems such as water shortage, clay swelling, and fluid backflow problems caused by traditional water-based fracturing fluid [7–10].

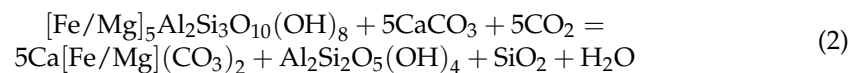
Due to its low viscosity and high diffusion ability, SC-CO<sub>2</sub> can easily penetrate deeply into the inner micro-pores of the reservoir during CO<sub>2</sub> waterless fracturing. The experiments conducted in different laboratories have clearly indicated the fact that using SC-CO<sub>2</sub> fracturing phase can reduce the fracture pressure and create multi-branch fracture networks [11–13].

However, when the SC-CO<sub>2</sub> is pumped into the shale reservoir, there also exists a complex chemical interaction process considering the formation water acidizing. The SC-CO<sub>2</sub>-water-rock interaction causes mineral dissolution and new mineral precipitation, and then leading to changes in the pore structure [14–22]. The reaction equation of CO<sub>2</sub>-water and different minerals is as follows:

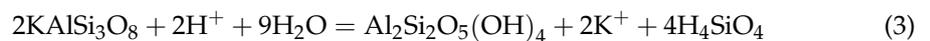
CO<sub>2</sub> Dissolution in formation water:



The reaction of CO<sub>2</sub> and chlorite:



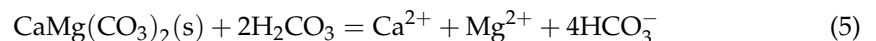
The reaction of potassium feldspar and H<sub>2</sub>O:



The reaction of CO<sub>2</sub> and calcite:



The reaction of CO<sub>2</sub> and dolomite:



Research results show that some minerals, such as calcite and dolomite, dissolve directly into the carbonic acid solution, resulting in the pore throat expansion. In contrast, some minerals, such as chlorite and potassium feldspar, also form new minerals when dissolved in a carbonic acid solution, such as kaolinite and iron/magnesium dolomite Ca[Fe/Mg](CO<sub>3</sub>)<sub>2</sub>, which exert uncertain influences on pores [13,17,18,22–26].

In the process of shale reservoir SC-CO<sub>2</sub> fracturing, the mineral composition of the shale is the important factor considering CO<sub>2</sub>-water-rock interaction. Previous studies conducted experimental research mainly under static, fixed period, and gas CO<sub>2</sub> conditions. The SC-CO<sub>2</sub> fracture and flow-back processes are typically supercritical and dynamic conditions. This paper presents a series of novel static and dynamic experiments to investigate the mechanisms and characteristics of different shales under SC-CO<sub>2</sub> condition and explore its potential impact on fracturing flowback timing.

## 2. Materials and Methods

The downhole samples were collected from the C7 and S1 formations in Ordos Basin, China. The rocks' colors were light green and black-gray for C7 and S1, respectively, as shown in Figure 1. Mineral and clay compositions were analyzed by using a Rigaku Miniflex II X-ray diffractometer. Results show that the mineral components are mainly quartz and clay, with some containing a small amount of calcite, dolomite, and siderite

(Figure 2). While clay mineral analysis indicates that 30% chlorite is present in the C7 formation, in contrast no chlorite was found in the S1 formation (Figure 3).



Figure 1. Downhole samples from C7 and S1 formation.

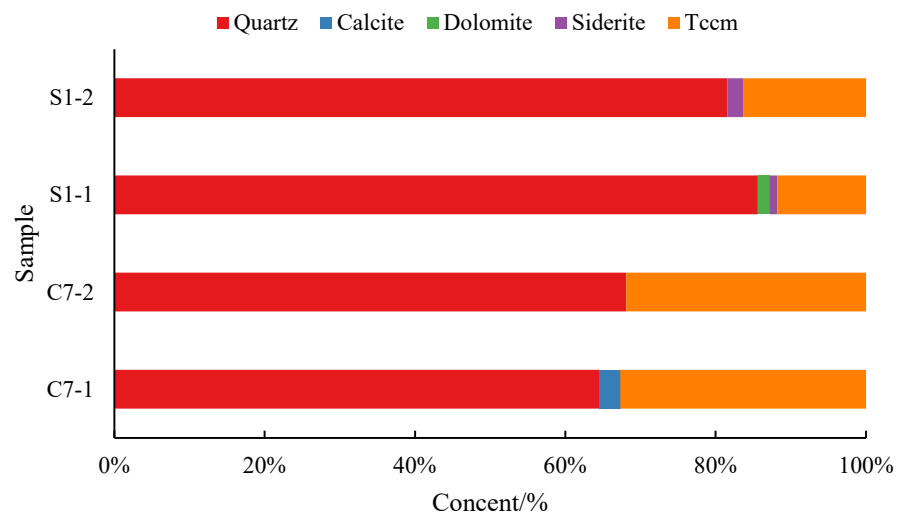


Figure 2. Rock mineral analysis of C7 and S1 shales.

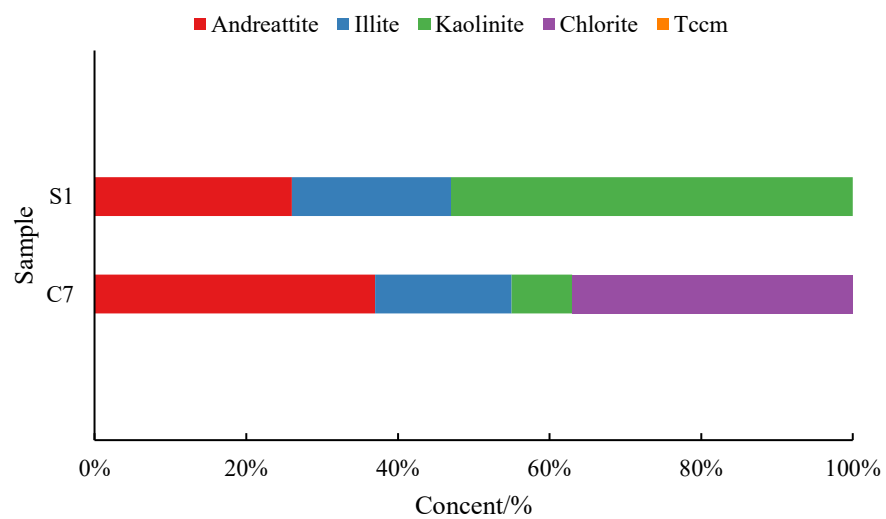


Figure 3. Clay mineral analyses of C7 and S1 shales.

### 2.1. Formation Water and Experiment Conditions

The formation water ion composition is shown in Table 1. The pH of the formation water is 6.0. According to well logging data [27], the burial depth of C7 and S1 formations is 2800–3500 m, and the reservoir temperature is 90–110 °C. The CO<sub>2</sub> injection pressure is set to 14 MPa according to the field and laboratory conditions. These parameters correspond to the SC-CO<sub>2</sub>, defined by the phase diagram of CO<sub>2</sub> (Figure 4).

**Table 1.** The formation water ion concentration.

Ions	Na <sup>+</sup>	K <sup>+</sup>	Ca <sup>2+</sup>	Mg <sup>2+</sup>	Cl <sup>-</sup>	SO <sub>4</sub> <sup>2-</sup>	HCO <sub>3</sub> <sup>-</sup>
concentration mg/L	13,302	525	1248	176	23,419	210	221

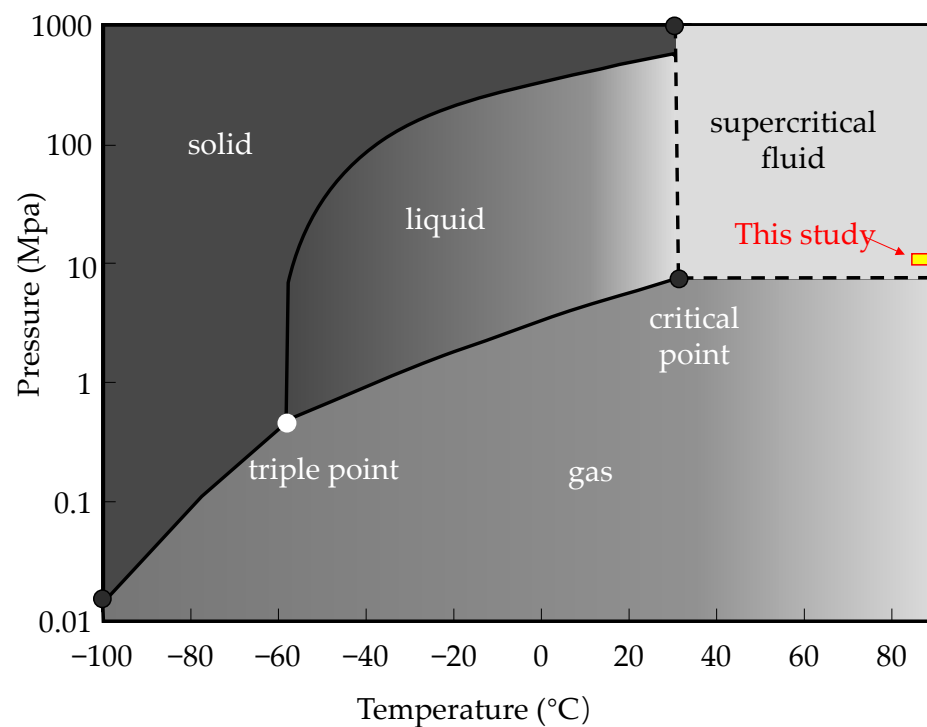


**Figure 4.** Phase diagram of CO<sub>2</sub>.

### 2.2. Static SC-CO<sub>2</sub>-Water-Rocks Interaction

The purity of the CO<sub>2</sub> gas used for the experiment was about 99.99%. The CO<sub>2</sub>-water-rock static experiment reaction vessel is a high-temperature and high-pressure autoclave, with a volume of 1 L, maximum pressure of 25 MPa, and a temperature range of 0–200 °C. Since the maximum pressure of the CO<sub>2</sub> cylinder is about 7 MPa, it is necessary to use a pressurization pump to compress the CO<sub>2</sub> and increase the pressure to 14 MPa. The autoclave heating system controls the reaction temperature. The temperature and pressure inside the autoclave are measured in real-time by a thermocouple and a pressure gauge, respectively. The static testing samples are approximately 2 cm<sup>3</sup> small cubic blocks, these small blocks are machined from the waste of the downhole shale sample after coring (the samples in static SC-CO<sub>2</sub> immersed experiments and the standard cores in dynamic experiments are from the same downhole bigger cores). The small block samples are placed in a high-temperature autoclave under SC-CO<sub>2</sub> conditions to react with formation water for 48 h. Figure 5 shows the experimental pictures of the autoclave, formation water, and rock samples.

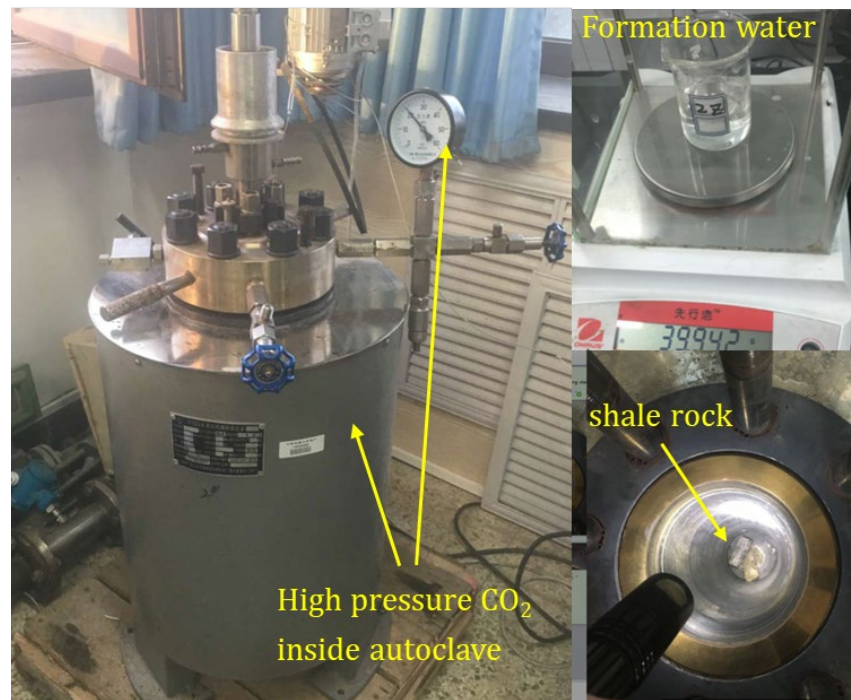


Figure 5. High-temperature and high-pressure autoclave.

### 2.3. Dynamic SC-CO<sub>2</sub> Injection Experiment

The dynamic displacement experimental device is mainly composed of two 1 L high temperature and high-pressure cylindrical storage tanks, metal core holders, SC-CO<sub>2</sub> resistant rubber sleeves, double cylinder high-pressure and constant pressure/flow metering pumps, a temperature control system, a confining pressure pump, inlet and outlet pressure sensors, a back pressure pump, and a back pressure valve. The schematic and the physical diagram of the dynamic displacement experimental set-up is shown in Figure 6.

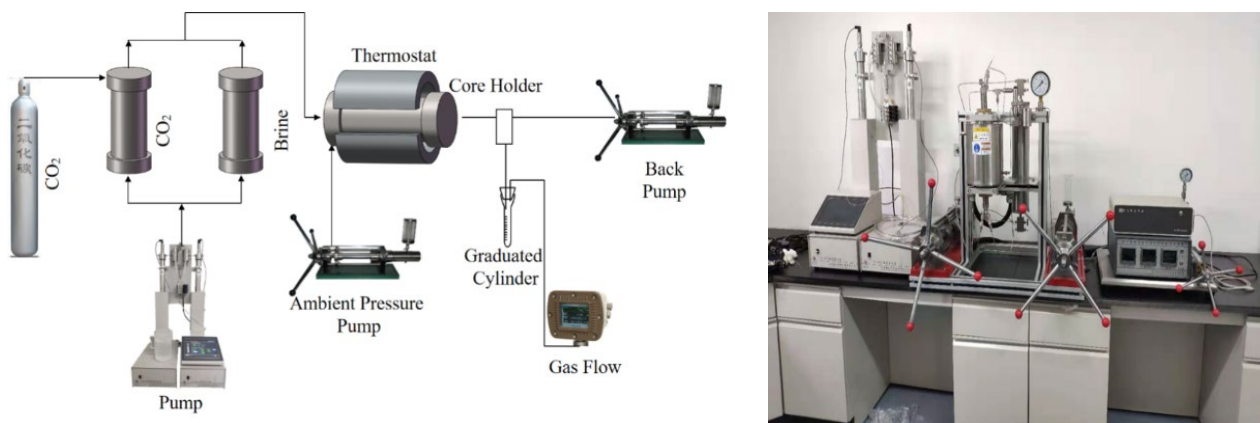


Figure 6. Schematic diagram and picture of the dynamic displacement experimental set-up.

The reaction temperature of the dynamic experiment is 100 °C, and the injection pressure remains constant at 14 MPa, which is consistent with the static experiment. The confining pressure is 17 MPa.

The standard core is placed in the core holder, then SC-CO<sub>2</sub> and formation water are injected into the core to determine the optimal flowback time after CO<sub>2</sub> fracturing. The experimental procedure is shown in Figure 7, the experiments are classified into long-interval displacement and short-interval displacement. Two standard samples (25 mm in diameter and 50 mm in length) coring from the downhole bigger core were prepared for

each shale. The cores were taken every 24 h in the long-interval experiment to measure the core porosity and permeability, and the total experiment duration was 48 h. In the short-interval experiment, porosity and permeability were measured every 6 h, and the total experiment duration was 24 h.

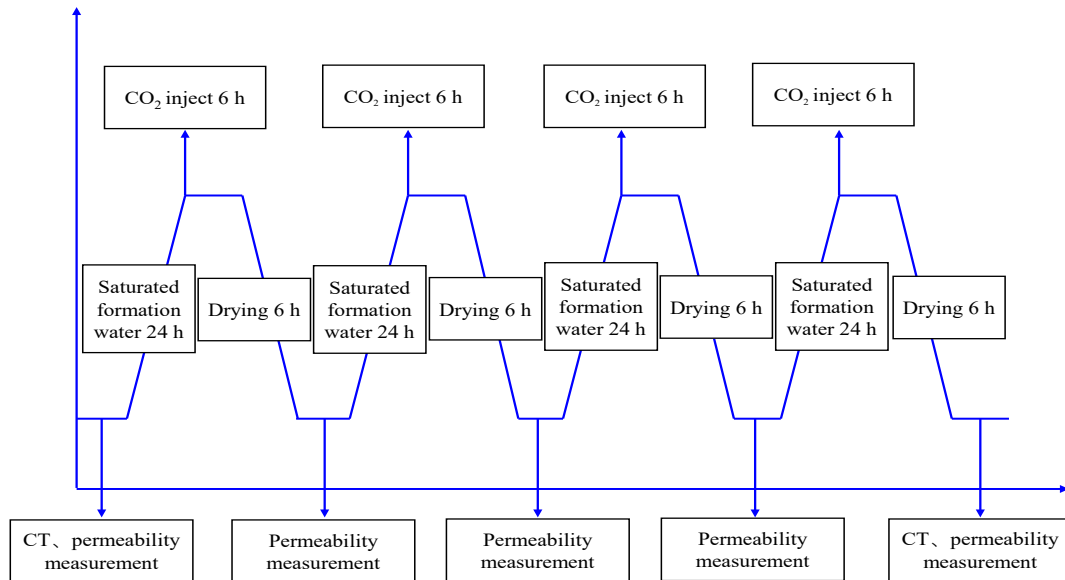


Figure 7. Dynamic reaction experiment procedure.

2.4. Measurements of Porosity and Permeability

The permeability of shale rock is tested using an ultra-low permeameter. In actual field operations, the injection direction of CO<sub>2</sub> fracturing is opposite to the production direction of the oil well (Figure 8). Therefore, the dynamic experiment adopts a method that injects CO<sub>2</sub> into one side of the rock core. It measures the porosity and permeability of core from the opposite direction while ensuring that the measurements of the confining and displacement pressures are the same.

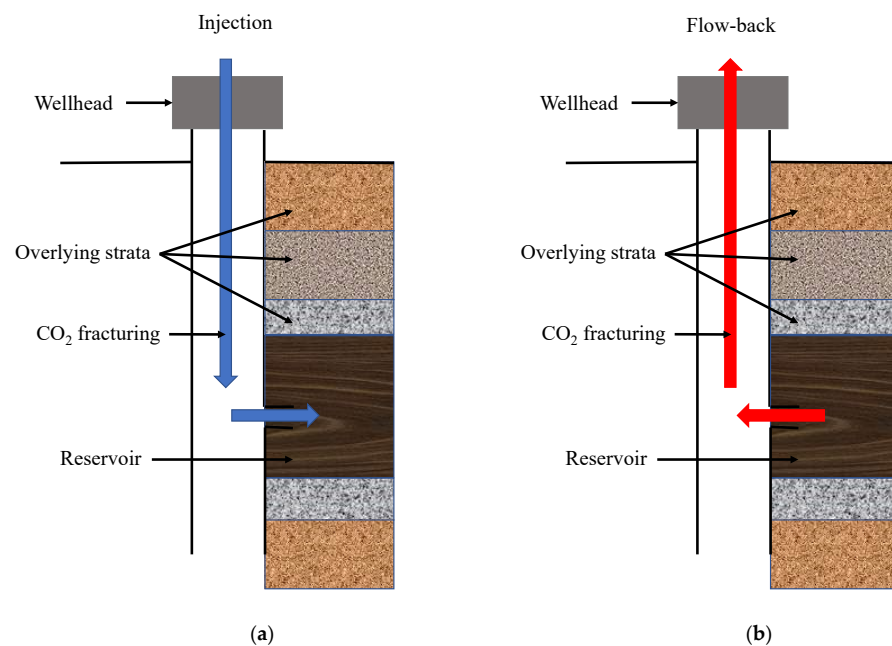


Figure 8. Schematic diagram of CO<sub>2</sub> fracturing and flow-back operations. (a) CO<sub>2</sub> fracturing. (b) Flow-back.

The helium porosimeter is a commonly used instrument for measuring pore volume. Its design principle is based on Boyle's law, where the temperature and volume of the core chamber are fixed. The measured sample volume, the core chamber, and the pores of the rock sample increase the equilibrium pressure. According to the volume of the calibration block and the standard equilibrium pressure curve, the equilibrium pressure of the inserted core sample is measured, and the reverse calculation volume of the rock skeleton and the porosity is obtained.

On the other hand, permeability refers to the rock body allowing fluid to pass through the ends of the rock. The principle of the equipment used in this experiment is the transient pressure pulse method. A sealed container is placed at both ends of the rock sample, and the pressures at the ends of the rock sample and the core chamber are balanced. A pressure pulse is given to one end of the container and gradually transferred across the core to the other. The computer monitors the pressure changes at both ends in real-time until the pressure is balanced again and calculated according to the upstream and downstream pressure drop curves.

When measuring permeability, note that the measurement should be consistent each time before and after the reaction. Measurement results at different confining and displacement pressures have no comparative value.

#### 2.5. Scanning Electron Microscopy (SEM) and X-ray Diffraction (XRD) Analysis

The surface texture and morphology of the rock were observed using a TM3030 SEM. The SEM is equipped with an energy dispersive spectroscopy system (EDS). The mineralogy of the rock samples is determined using X-ray diffraction analysis (Rigaku Miniflex II X-Ray Diffractometer). Measurement was performed within the angular range of 3–45° at a scanning speed of  $2\theta = 1^\circ/\text{min}$ . The diffraction data were processed using the MDI software (known as the JADE). The detailed procedures follow the "Analysis Method for Clay Minerals and Ordinary Non-Clay Minerals in Sedimentary Rocks by X-Ray Diffraction (SY/T5163-2010)".

#### 2.6. CT Scanning

The core is scanned using a CT scanner (GE Brivo CT385 double-slice spiral CT scanner) and median filter processing for the CT image of the core then identified the pores in the image. The change in axial and radial porosity of core samples is calculated. Moreover, the change in pore structure before and after the reaction is compared.

The 2D CT slice images can be used to reconstruct the 3D core according to the gray value between the rock pore and skeleton. In this study, about 160 slice images are scanned continuously for each sample along the core's length. Six slices before and after reconstructions are removed to avoid possible boundary effects that could occur at both ends of the rock CT scanning process. System noise is generated in the process of CT scanning due to the sample thickness and the number of large and small X-ray photons. It affects the quality of the gray image, segmentation processing of the core pore skeleton, and quantitative analysis of porosity. After the noise reduction process, the pore and the core skeleton grayscales are determined.

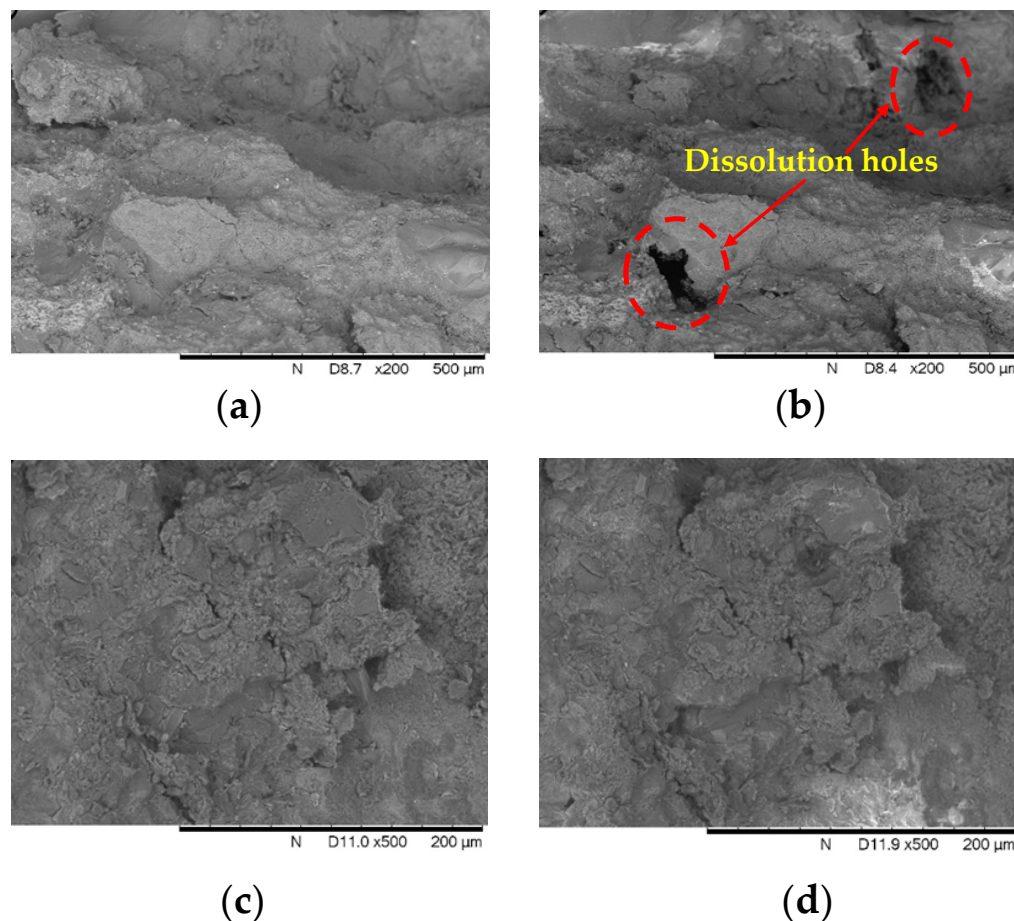
### 3. Results and Analysis

#### 3.1. Static SC-CO<sub>2</sub>-Water-Rock Interaction

##### 3.1.1. Changes in Morphology

SC-CO<sub>2</sub>-water-rock static reactions are evaluated by electron microscopy of cores to observe the changes in microstructure at the exact location before and after the reaction (the block samples were marked with a marker on the surface in order to navigate and observe the same micro area before and after the reaction). Some of the minerals on the surface of the C7 core are dissolved and appear in dissolution holes (Figure 9b). Based on the clay mineral analysis result (Figure 3) and chemical reaction Equation (2), the C7 sample is rich in chlorite. It easily reacts with carbonate formation water to form new minerals.

However, there is no significant difference in the core sample of the S1 before and after the reaction. No large amounts of mineral dissolution are found on the surface of the core sample (Figure 9c,d).

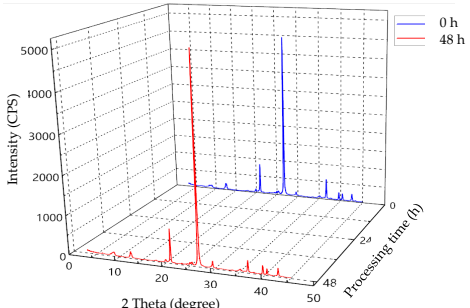
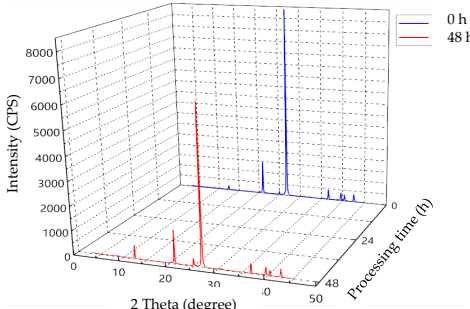


**Figure 9.** SEM comparison of rock before and after the reaction. (a) C7 sample before the reaction. (b) C7 sample (Dissolution hole). (c) S1 sample before the reaction. (d) S1 sample after reaction (No big difference).

### 3.1.2. Changes in Mineral Compositions

XRD analysis of core samples before and after the reaction shows that the clay mineral content of the C7 sample decreases obviously. At the same time, there is almost no change in the S1 core sample (Table 2). Combined with the results of SEM, it can be found that clay minerals dissolution reactions cause clay minerals to decrease from 32.7% to 24.7%. Although quartz does not react with carbonated formation water, the decrease in clay minerals increases the proportion of quartz content (from 64.5% to 71.6%).

**Table 2.** Mineral types and contents analyzed by XRD.

Samples	XRD Analysis	Time	Mineral Type and Content, wt%				
			Quartz	Calcite	Dolomite	Siderite	TCCM
C7		0 h	64.5	2.8	/	/	32.7
		48 h	71.6	3.7	/	/	24.7
S1		0 h	85.6	/	1.6	1.0	11.8
		48 h	87.3	/	2.9	0	9.8

### 3.2. Dynamic SC-CO<sub>2</sub> Injection Experimental Results

#### 3.2.1. Change in Porosity and Permeability of the Long-Interval Testing

The change in permeability for long-interval (24 h) experiments is shown in Figure 10. The permeability of the C7 core decreases during the first 24 h, from the initial value of  $0.14 \times 10^{-3} \mu\text{m}^2$  to the minimum value of  $0.11 \times 10^{-3} \mu\text{m}^2$ , and then increases to the final value of  $0.13 \times 10^{-3} \mu\text{m}^2$  by the end of 48 h. The maximum permeability change is around 21.4% compared to the initial permeability. The change in permeability is mainly caused by the new mineral sediment, which blocks the pore throat and decreases permeability. With the continuous injection of SC-CO<sub>2</sub>, some sediments are drained, and the permeability increases. However, the S1 core almost keeps stable during the experiment. From the initial value of  $0.011 \times 10^{-3} \mu\text{m}^2$  to the middle of  $0.012 \times 10^{-3} \mu\text{m}^2$ , and then end with  $0.012 \times 10^{-3} \mu\text{m}^2$ . The permeability change is less than 9%. The CO<sub>2</sub>-water-rock interaction has little influence on the S1 rock permeability.

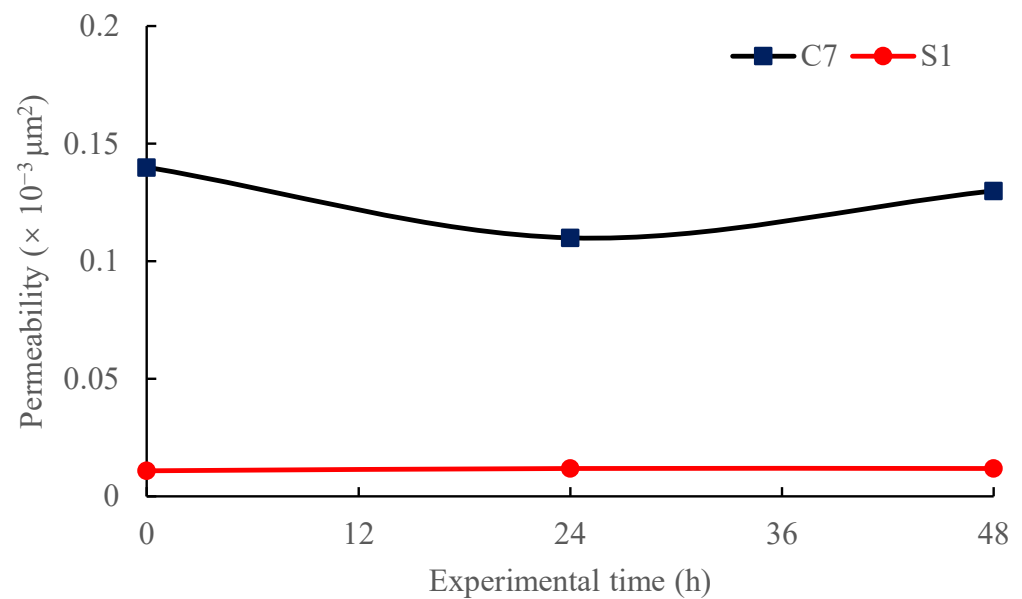


**Figure 10.** Permeability changes of long-interval (24 h) experiment.

The change in porosity for long-interval (24 h) experiments is shown in Figure 11. The porosity of the C7 core decreases at the beginning stage and reaches a minimum value of 2.17% at 24 h and then increases to 3.25% by the end of 48 h. Compared with the initial porosity, the final porosity of the C7 core decreased by 36.5%. After the dissolution, the weakly cemented mineral particles that are released migrate into the core. However, the deposition is greater than the dissolution. Compared with the C7 core, the S1 core has almost no minerals dissolved. The cementation condition is good, and there is almost no migration of weakly cemented minerals. Combined with the static experiment results (Figure 9c,d), it can be considered that the  $\text{CO}_2$ -water-rock interaction hardly occurs in the S1 core.

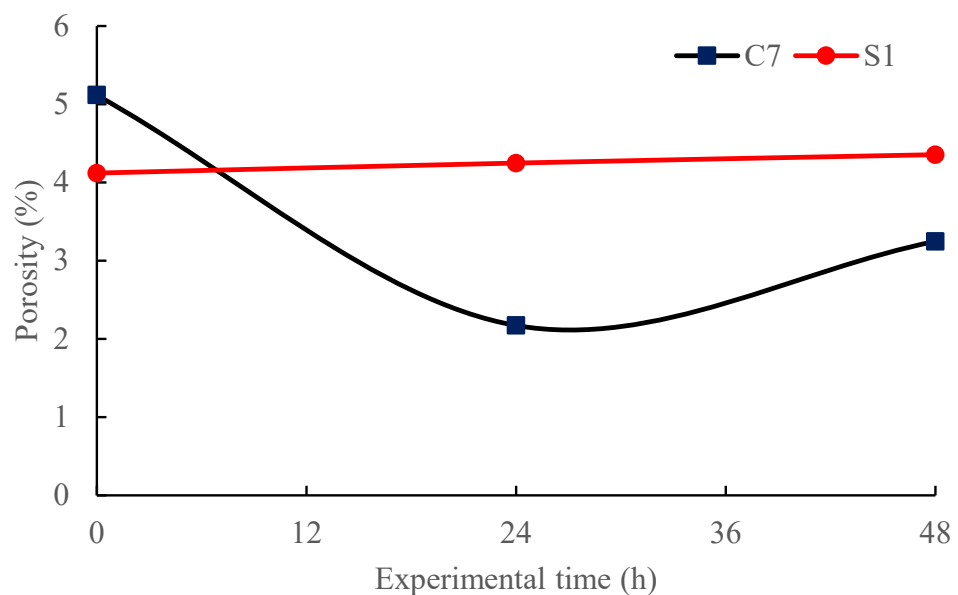


**Figure 11.** Porosity changes of long-interval (24 h) experiment.

### 3.2.2. Change in Porosity and Permeability of the Short-Interval Testing

For the short-interval (6 h) dynamic experiments, the permeability and porosity changes are shown in Figures 12 and 13, respectively. The C7 core permeability gradually decreases to the minimum value of  $0.037 \times 10^{-3} \mu\text{m}^2$  at 12 h. Finally, it increases to  $0.043 \times 10^{-3} \mu\text{m}^2$ , but it is still smaller than the initial value of  $0.052 \times 10^{-3} \mu\text{m}^2$ . S1 core permeability increases to the maximum value of 0.015 at 6 h and then decreases to a stable value of  $0.01 \times 10^{-3} \mu\text{m}^2$ . The variation regulars of porosity are similar to the permeability. The porosity of the C7 core decreases from the initial value of 5.328% to the minimum of 4.265% and then gradually increases to 4.724%. Similar to the permeability, the S1 core porosity reaches a peak of 5.468% at 6 h, and then dramatically decreases to the bottom at 4.69%.

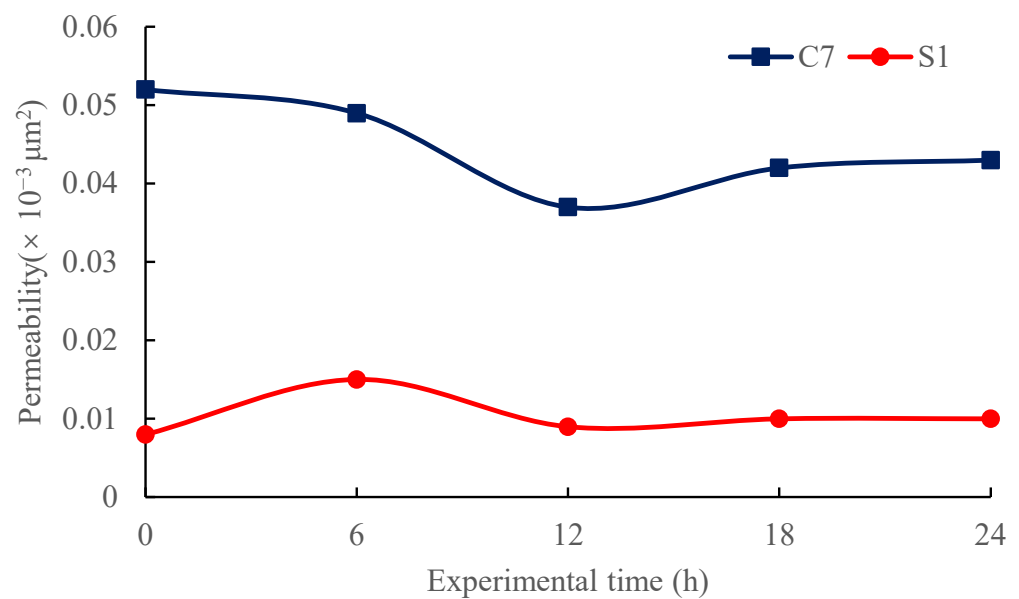


Figure 12. Permeability changes of short-interval (24 h) experiment.

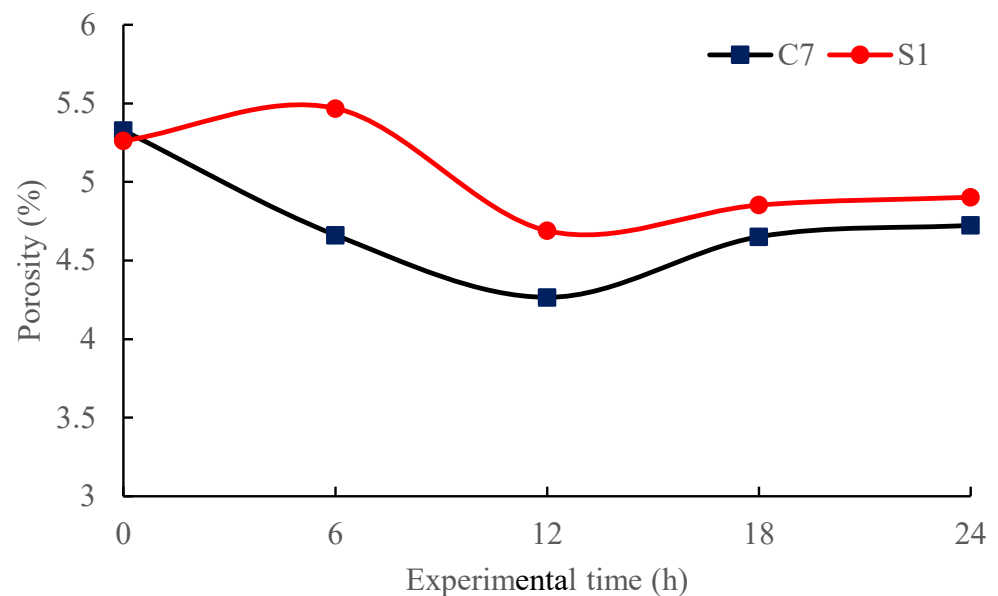


Figure 13. Porosity changes of short-interval (24 h) experiment.

Combining the long-interval and short-interval experiment results, it can be shown that the minimum value of permeability and porosity of the C7 cores appears at 24 h in the long-interval experiment, but in the short-interval experiment, the minimum values move ahead to 12 h. The difference in the initial permeability is related to the core structure, such as micro-cracks. However, the similar change trend reflects the effect of the CO<sub>2</sub>-water-rock reaction process. The most serious reservoir seepage damage time is between 12 and 24 h during the SC-CO<sub>2</sub> injection. Fracturing SC-CO<sub>2</sub> flowback time recommended before 12 h or after 24 h. Between 12 h and 24 h, flowback operation could cause SC-CO<sub>2</sub> retention.

For the S1 core results, the porosity and permeability change little in the long interval experiment. However, in the short interval experiment, the physical properties of S1 change more obviously, and both permeability and porosity appear a peak value at 6 h. Generally, there is no strict flow-back time requirement for the S1 reservoir during SC-CO<sub>2</sub> fracturing, but it may get a better flow-back result around 6 h.

### 3.2.3. CT Scanning 3D Digital Reconstruction and Micro Blocking Analysis

The core slice data is obtained by CT scanning of the core before and after the CO<sub>2</sub>-water-rock reaction. The porosity distribution of C7 and S1 cores after 3D digital reconstruction is shown in Figure 14. The helium porosimeter measured porosity of the C7 core is 5.35%. The reconstructed pore volume is 900,008 μm<sup>3</sup> and the porosity is 5.38%. The CT reconstruction porosity is basically consistent with that of the helium porosimeter. In Figure 14a, the C7 core has uniform pore distribution and good cementation. After the CO<sub>2</sub>-water-rock interaction, the helium porosimeter measured porosity is 4.71%. The CT reconstructed pore volume is 875,941 μm<sup>3</sup> and the porosity is 4.90%. The porosity decreased by 0.64% compared to the initial. By comparing the CT digital slice porosities as shown in Figure 14c, the porosity is slightly reduced by the CO<sub>2</sub>-water-rock interaction along the core length. Nevertheless, on the outlet side (dash square in Figure 14c), high-pressure CO<sub>2</sub> flooding pushes the newly forming minerals particles to migrate to the outlet side and block the pore throat.

The helium porosimeter measured porosity of the S1 core is 5.28%. The reconstructed pore volume is 993,307 μm<sup>3</sup>, and the porosity reconstructed by CT scan is 5.37%. In Figure 14d, the pore distribution of the S1 core is uneven. After the CO<sub>2</sub>-water-rock reaction, the helium porosimeter measured porosity is 4.97%. The reconstructed pore volume is 955,682 μm<sup>3</sup> and the porosity is 5.08%. In Figure 14f, the porosity change of the S1 core is not obvious before and after the CO<sub>2</sub> injection, which indicates that the pore throat of the core is almost not affected by the CO<sub>2</sub>-water-rock interaction. CT scanning analysis can clearly explain the permeability and porosity testing results.

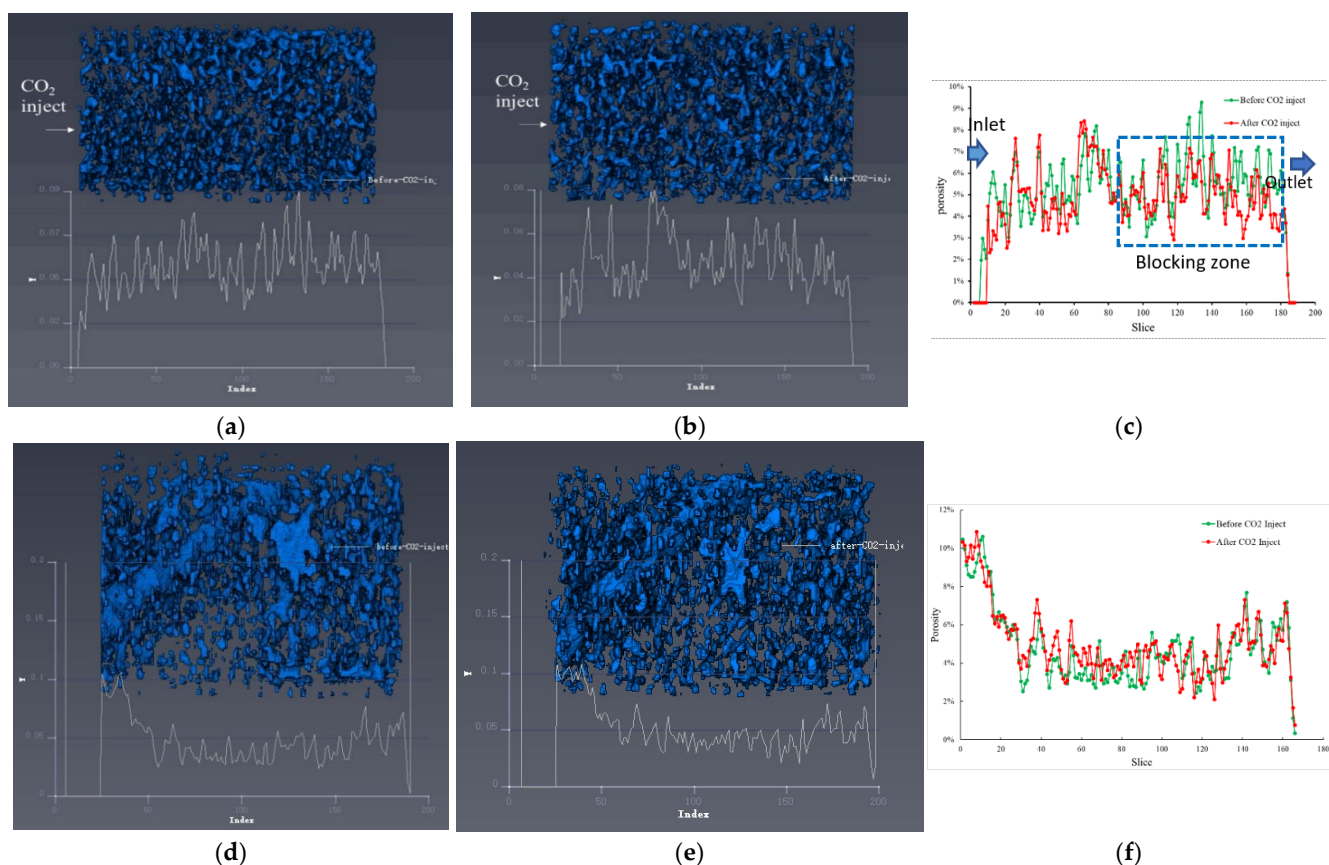


**Figure 14.** Comparison of porosity distribution. (a) C7 core before interaction. (b) C7 core after interaction. (c) Change of C7 core porosity. (d) S1 core before interaction. (e) S1 core after interaction. (f) Change of S1 core porosity.

#### 4. Conclusions

In this study, two kinds of shale rock reacting with SC-CO<sub>2</sub> under static and dynamic experimental conditions were investigated. The surface morphologies, newly formed minerals, porosity, and permeability of the reservoir rocks before and after the interaction were studied. The main conclusions are as follows:

- (1) From the static experiment, dissolution and precipitation can be observed, which shows that SC-CO<sub>2</sub> and water will certainly change the physical properties of the shale rocks in the C7 and S1 formations. Dissolution happens to minerals such as dolomite and chlorite in the rock; the precipitation is caused by the iron dolomite formed by the reaction of chlorite with calcium carbonate and carbon dioxide.
- (2) The reconstruction of pores before and after the dynamic experiment was analyzed by CT scanning. The CO<sub>2</sub>-water-rock interaction may lead to the blocking of small pores. Compared with the S1 core, SC-CO<sub>2</sub> flooding pushes the newly formed mineral particles to migrate to the outlet side and block the pore throat in the C7 core.
- (3) The research results show that the S1 reservoir is basically not affected by the CO<sub>2</sub>-water-rock interaction, and the flow back is the best within 6 h after SC-CO<sub>2</sub> injection.
- (4) The C7 reservoir is most severely affected by the CO<sub>2</sub>-water-rock interaction in 12–24 h. It is recommended to perform the flow back within 12 h or after 24 h, improper flowback strategies could cause SC-CO<sub>2</sub> retention and reservoir damage.

**Author Contributions:** Conceptualization, W.Y.; Methodology, W.Y. and W.L.; Investigation, W.Y. and G.L.; Resources, T.W.; Writing—original draft, G.L. and W.L.; Writing—review & editing, W.Y., M.S., J.P.E.A.N. and K.M.; Funding acquisition, T.W. All authors have read and agreed to the published version of the manuscript.

**Funding:** This research was supported by the National Natural Science Foundation Project (Grant No. 52274015) & Open Research Fund Program of Key Laboratory of Metallogenic Prediction of Nonferrous Metals and Geological Environment Monitoring (Central South University), Ministry of Education (2019YSJS06).

**Data Availability Statement:** Not applicable.

**Acknowledgments:** We thank Fujian Zhou from the Center for Reservoir Stimulation, China University of Petroleum (Beijing), for help with the CT scanning and Changqing Oilfield Company for providing samples of rock.

**Conflicts of Interest:** The authors declare that there are no conflicts of interest.

## References

1. Ely, J.W.; Fowler, S.A.; Tiner, R.L.; Aro, D.J.; Sicard, G.R.; Sigman, T.A. "Slick water fracturing and small proppant" The future of stimulation or a slippery slope. In Proceedings of the SPE Annual Technical Conference and Exhibition, Amsterdam, The Netherlands, 27–29 October 2014; Society of Petroleum Engineers: Amsterdam, The Netherlands, 2014; p. 12.
2. Shafer, M.T. Are slick water-fracturing applications effective in the j-sand formation? In Proceedings of the SPE Annual Technical Conference and Exhibition, Dallas, TX, USA, 9–12 October 2005; Society of Petroleum Engineers: Dallas, TX, USA, 2005; p. 13.
3. Im, H.; Jang, H.; Topal, E.; Nehring, M. Long- and short-term strategies for estimation of hydraulic fracturing cost using fuzzy logic. *Minerals* **2022**, *12*, 715. [[CrossRef](#)]
4. Astafyev, V.; Lushev, M.; Mitin, A.; Plotnikov, A.; Mironov, E.; Legay, A.; Zolnikov, D. Multistage hydrocarbon-based fracturing in tight gas formation (Russian). In Proceedings of the SPE Russian Petroleum Technology Conference, Virtual, 26–29 October 2020; p. 22.
5. Dalrymple, E.D.; Eoff, L.S.; Everett, D.M. Conformance while fracturing tight gas formations. In Proceedings of the SPE Tight Gas Completions Conference, San Antonio, TX, USA, 9–11 June 2008; Society of Petroleum Engineers: San Antonio, TX, USA, 2008; p. 12.
6. Murtaza, M.; Al Naeim, S.; Waleed, A. Design and evaluation of hydraulic fracturing in tight gas reservoirs. In Proceedings of the SPE Saudi Arabia Section Technical Symposium and Exhibition, Al-Khobar, Saudi Arabia, 9–11 May 2013; Society of Petroleum Engineers: Al-Khobar, Saudi Arabia, 2013; p. 10.
7. Almubarak, M.; Almubarak, T.; Ng, J.H.; Hernandez, J.; Nasr-El-Din, H. Recent advances in waterless fracturing fluids: A review. In Proceedings of the Abu Dhabi International Petroleum Exhibition & Conference, Abu Dhabi, United Arab Emirates, 9–12 November 2020; Society of Petroleum Engineers: Abu Dhabi, United Arab Emirates, 2020; p. 25.
8. Cui, W.; Cui, M.; Wang, C.; Liang, C. Waterless stimulation for unconventional resources: An alternative to conventional water-based fracturing techniques. In Proceedings of the Abu Dhabi International Petroleum Exhibition & Conference, Abu Dhabi, United Arab Emirates, 13–16 November 2017; Society of Petroleum Engineers: Abu Dhabi, United Arab Emirates, 2017; p. 14.
9. Qinghai, Y.; Siwei, M.; Tao, F.; Yongwei, D.; Shi, C. Well and layer selection method study of CO<sub>2</sub> waterless fracturing. In Proceedings of the SPE Kingdom of Saudi Arabia Annual Technical Symposium and Exhibition, Dammam, Saudi Arabia, 23–26 April 2018; Society of Petroleum Engineers: Dammam, Saudi Arabia, 2018; p. 9.
10. Wang, C.; Cui, W.; Zou, H.; Wang, C.; Zhang, X. Waterless stimulation: CO<sub>2</sub> fracturing technology in unconventional resources. In Proceedings of the International Petroleum Technology Conference, Dhahran, Saudi Arabia, 13 January 2020; p. 9.
11. Tao, L.; Han, J.; Feng, Y.; McLennan, J.D. Study on the alteration of pore parameters of shale with different natural fractures under supercritical carbon dioxide seepage. *Minerals* **2022**, *12*, 660. [[CrossRef](#)]
12. Lyu, Q.; Long, X.; Ranjith, P.G.; Tan, J.; Kang, Y.; Wang, Z. Experimental investigation on the mechanical properties of a low-clay shale with different adsorption times in sub-/super-critical CO<sub>2</sub>. *Energy* **2018**, *147*, 1288–1298. [[CrossRef](#)]
13. Olabode, A.; Radonjic, M. Fracture conductivity modeling in experimental shale rock interactions with aqueous CO<sub>2</sub>. *Energy Procedia* **2017**, *114*, 4494–4507. [[CrossRef](#)]
14. Bizhani, M.; Ardakani, O.H.; Hawthorne, S.B.; Cesar, J.; Kurz, B.; Percival, J.B. CO<sub>2</sub>-enhanced oil recovery mechanism in Canadian Bakken Shale. *Minerals* **2022**, *12*, 779. [[CrossRef](#)]
15. Ali, M.; Hascakir, B. Water-rock interaction for Eagle Ford, Marcellus, Green River, and Barnett Shale samples. In Proceedings of the SPE Eastern Regional Meeting, Morgantown, WV, USA, 13–15 October 2015; Society of Petroleum Engineers: Morgantown, WV, USA, 2015; p. 16.
16. Ali, M.; Hascakir, B. Water/rock interaction for Eagle Ford, Marcellus, Green River, and Barnett Shale samples and implications for hydraulic-fracturing-fluid engineering. *SPE J.* **2017**, *22*, 162–171. [[CrossRef](#)]
17. Egermann, P.; Bazin, B.; Vizika, O. An experimental investigation of reaction-transport phenomena during CO<sub>2</sub> injection. In Proceedings of the SPE Middle East Oil and Gas Show and Conference, Manama, Kingdom of Bahrain, 12–15 March 2005; Society of Petroleum Engineers: Manama, Kingdom of Bahrain, 2005; p. 10.
18. Shiraki, R.; Dunn, T.L. Experimental study on water-rock interactions during CO<sub>2</sub> flooding in the Tensleep Formation, Wyoming, USA. *Appl. Geochem.* **2000**, *15*, 265–279. [[CrossRef](#)]

19. Wang, W.; Wei, W.; Leach, D.; Yan, C.; Spilker, K. Rock-fluid interaction and its application in unconventional production. In Proceedings of the SPE/AAPG/SEG Unconventional Resources Technology Conference, online, 20–22 July 2020; p. 18.
20. Wellman, T.P.; Grigg, R.B.; McPherson, B.J.; Svec, R.K.; Lichtner, P.C. Evaluation of CO<sub>2</sub>-brine-reservoir rock interaction with laboratory flow tests and reactive transport modeling. In Proceedings of the International Symposium on Oilfield Chemistry, Houston, TX, USA, 5–7 February 2003; Society of Petroleum Engineers: Houston, TX, USA, 2003; p. 9.
21. Wang, T.Y.; Tian, S.C.; Liu, Q.L.; Li, G.S.; Sheng, M.; Ren, W.X.; Zhang, P.P. Pore structure characterization and its effect on methane adsorption in shale kerogen. *Pet. Sci.* **2021**, *18*, 565–578. [[CrossRef](#)]
22. Li, H.B.; Yang, Z.M.; Li, R.S.; Zhou, T.Y.; Guo, H.K.; Liu, X.W.; Meng, H. Mechanism of CO<sub>2</sub> enhanced oil recovery in shale reservoirs. *Pet. Sci.* **2021**, *18*, 1788–1796. [[CrossRef](#)]
23. El-Hajj, H.; Odi, U.; Gupta, A. Carbonate reservoir interaction with supercritical carbon dioxide. In Proceedings of the International Petroleum Technology Conference, Beijing, China, 26–28 March 2013; p. 7.
24. Mohamed, I.M.; He, J.; Nasr-El-Din, H.A. Carbon dioxide sequestration in dolomite rock. In Proceedings of the International Petroleum Technology Conference, Bangkok, Thailand, 15 November 2011; International Petroleum Technology Conference: Bangkok, Thailand, 2011; p. 26.
25. Sun, Y.; Dai, C.; Yu, Z.; Xin, Y. The carbonic acid-rock reaction in feldspar/dolomite-rich tight and its impact on CO<sub>2</sub>-water relative permeability during geological carbon storage. *Chem. Geol.* **2021**, *584*, 120527. [[CrossRef](#)]
26. Khather, M.; Saeedi, A.; Rezaee, R.; Noble, R.R.; Gray, D. Experimental investigation of changes in petrophysical properties during CO<sub>2</sub> injection into dolomite-rich rocks. *Int. J. Greenh. Gas Control* **2017**, *59*, 74–90. [[CrossRef](#)]
27. Ju, W.; Niu, X.B.; Feng, S.B.; You, Y.; Xu, K.; Wang, G.; Xu, H.R. Predicting the present-day in situ stress distribution within the Yanchang Formation Chang 7 shale oil reservoir of Ordos Basin, central China. *Pet. Sci.* **2020**, *17*, 912–924. [[CrossRef](#)]